ACS NANO
Cite This: ACS Nano XXXX, XXX, XXX-XXX
www.acsnano.org

ARTICLE

Mid-Wave Infrared Photoconductors Based on Black Phosphorus-Arsenic Alloys

Matin Amani,[†,‡] Emma Regan,[†,‡] James Bullock,[†,‡] Geun Ho Ahn,[†,‡] and Ali Javey*[,†,‡]

[†]Electrical Engineering and Computer Sciences, University of California at Berkeley, Berkeley, California 94720, United States
[‡]Materials Sciences Division, Lawrence Berkeley National Laboratory, Berkeley, California 94720, United States

Supporting Information

ABSTRACT: Black phosphorus (b-P) and more recently black phosphorus-arsenic alloys (b-PAs) are candidate 2D materials for the detection of mid-wave and potentially long-wave infrared radiation. However, studies to date have utilized laser-based measurements to extract device performance and the responsivity of these detectors. As such, their performance under thermal radiation and spectral response has not been fully characterized. Here, we perform a systematic investigation of gated-photoconductors based on b-PAs alloys as a function of thickness over the composition range of 0−91% As. Infrared transmission and reflection measurements are performed to determine the bandgap of the various compositions. The spectrally resolved photoresponse for various compositions in this material system is investigated to confirm absorption measurements, and we find that the cutoff wavelength can be tuned from 3.9 to 4.6 μm over the studied compositional range. In addition, we investigated the temperature-dependent photoresponse and performed calibrated responsivity measurements using blackbody flood illumination. Notably, we find that the specific detectivity (D^*) can be optimized by adjusting the thickness of the b-P/b-PAs layer to maximize absorption and minimize dark current. We obtain a peak D^* of 6×10^{10} cm $Hz^{1/2}$ W^{-1} and 2.4×10^{10} cm $Hz^{1/2}$ W^{-1} for pure b-P and b-PAs (91% As), respectively, at room temperature, which is an order of magnitude higher than commercially available mid-wave infrared detectors operating at room temperature.

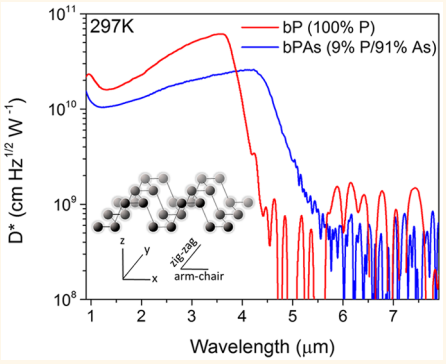

KEYWORDS: *2D materials, b-P, b-PAs, mid-wave infrared, photodetector, specific detectivity*

The detection of infrared (IR) light has numerous applications, including thermal imaging, gas sensing, and communication.[1−3] Thermal radiation falls in either the mid-wave (3−5 μm) or long-wave (8−14 μm) spectral bands. Research in detectors for these wavelengths has been dominated by thermal detectors such as bolometers and semiconductor detectors including indium antimonide, mercury cadmium telluride, or type-II quantum wells.[4−7] However, key challenges still exist in both detector types. Specifically, semiconductor detectors typically require cryogenic cooling and complex growth/fabrication processes leading to high costs.[8] On the other hand, while bolometers can achieve room temperature operation at significantly lower costs, they are ultimately limited by slow temporal response, limiting their applications.[7] The key challenge for semiconductor detectors operating in the mid- and long-wave IR bands is the significant thermal generation, which results from the small bandgap requirements (0.3 and 0.1 eV, respectively, for mid- and long-wave). This in turn results in significant dark currents due to thermal generation.

A potential route to mediate thermal generation within IR photodetectors is to minimize the thickness of the active electronic material. Two-dimensional (2D) materials have potential to accomplish this through both extreme reduction in thickness as well as the possibility of coupling to nano-optics to increase total absorption.[9,10] Furthermore, 2D materials have naturally passivated surfaces due to the lack of out-of-plane bonding, which can result in high interface quality in the presence of suitable defect passivation and can remove the requirement for a lattice matched substrate.[11−13] Significant research has been performed in this area, with much of the initial work focused on mono- and bilayer graphene; however, these devices suffer from low intrinsic absorption and high dark current due to the absence of a bandgap.[14−16] More recently black phosphorus (b-P) and black phosphorus-arsenic (b-PAs) alloys have emerged as potential 2D semiconductors with suitable bandgaps for IR detection.[17,18] In addition, b-P has been shown to provide other attractive properties, such as high mobility, anisotropic optical properties, and a highly tunable thickness-dependent direct-bandgap over the monolayer to six-layer range.[19−21] Previous studies have demonstrated both photoconductive as well as photovoltaic b-P photodetectors and have demonstrated that this material system shows high

Received: October 3, 2017
Accepted: October 31, 2017
Published: October 31, 2017

DOI: 10.1021/acsnano.7b07028
ACS Nano XXXX, XXX, XXX−XXX

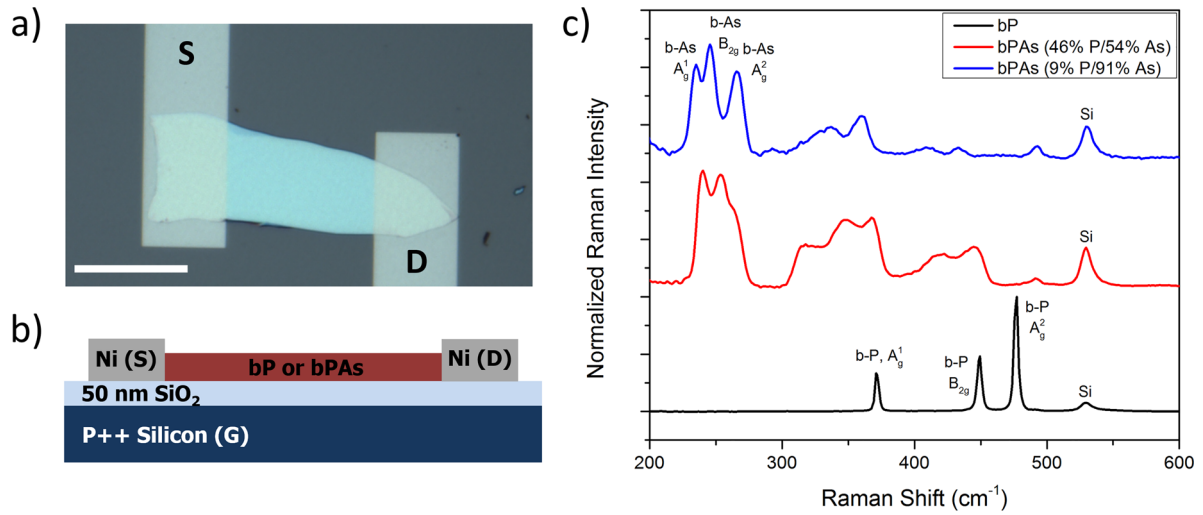

Figure 1. (a) Optical microscope image of a typical b-P gated photoconductor with a thickness of 29 nm; the scale bar is 10 μm. (b) Cross-sectional schematic of the gated photoconductor. (c) Raman spectra measured for pure b-P as well as b-PAs alloys.

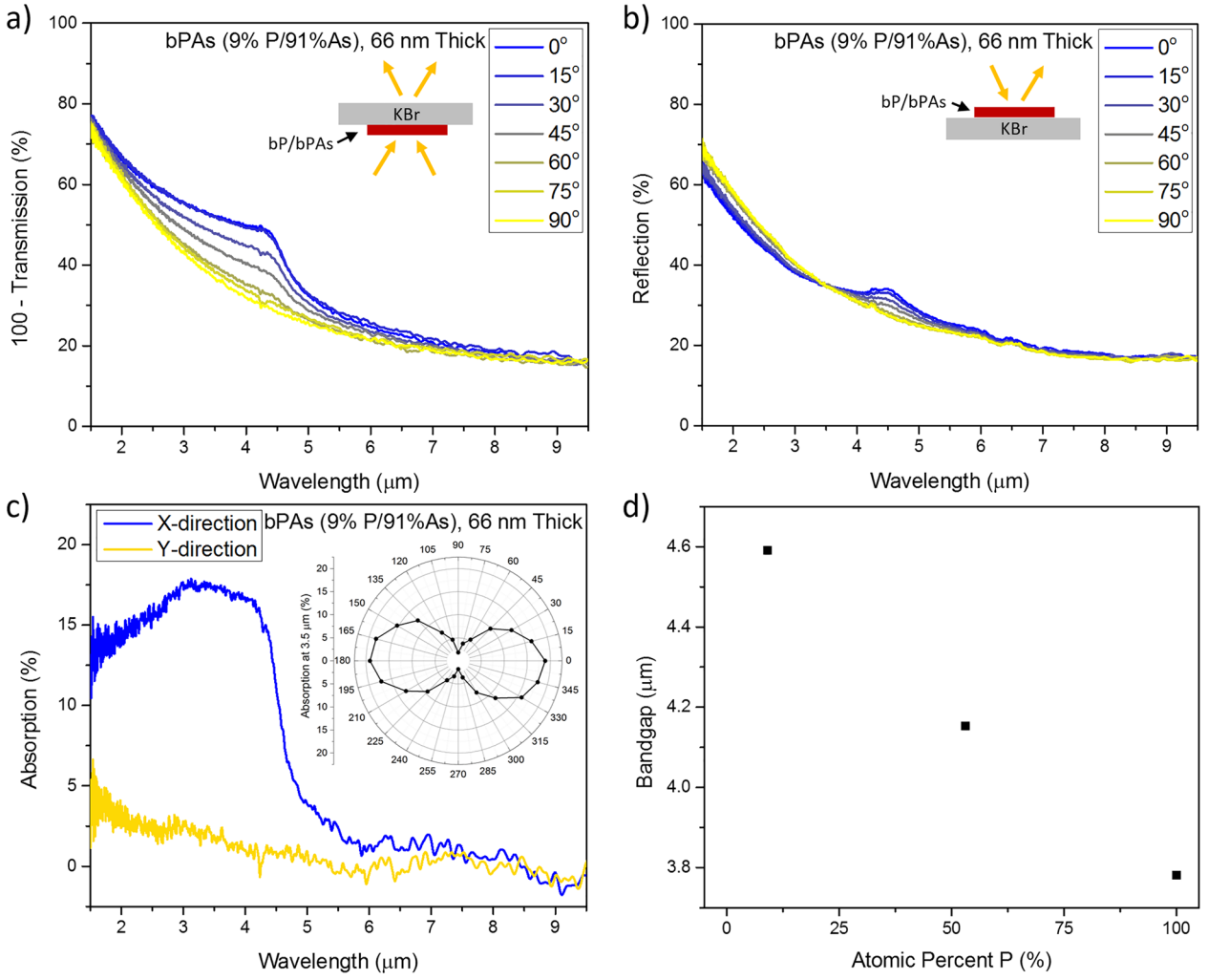

Figure 2. (a) Polarization resolved transmission spectra measured for a 66 nm-thick b-PAs crystal on a KBr substrate; inset shows the optical configuration used during measurements. (b) Polarization resolved reflection spectra measured for a 66 nm-thick b-PAs crystal on a KBr substrate; inset shows the optical configuration used during measurements. (c) Absorption spectra, calculated from 100-T−R, for the b-PAs crystal shown in (a) and (b) along both crystal directions. Inset shows the polarization resolved absorption at a wavelength of 3.5 μm. (d) Bandgap of b-P and b-PAs alloys as a function of P concentration.

DOI: 10.1021/acsnano.7b07028
ACS Nano XXXX, XXX, XXX−XXX

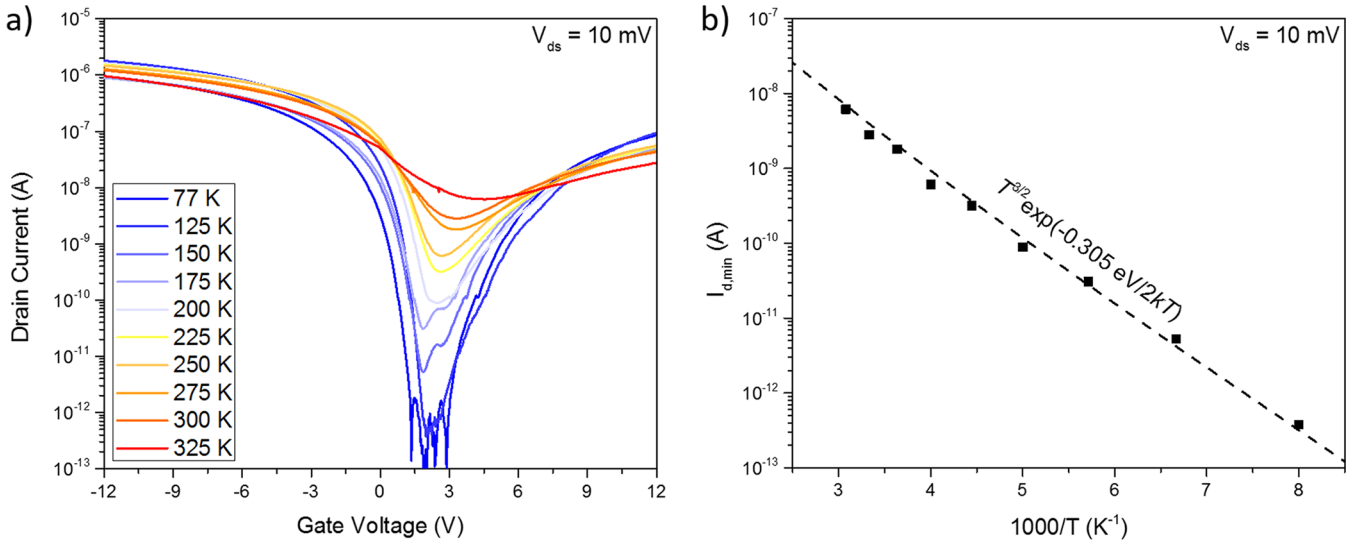

Figure 3. (a) Transfer characteristics of an 18 nm-thick b-P crystal measured as a function of temperature at a drain bias of 10 mV. Note that a cold shield was utilized for these measurements. (b) Arrhenius plot of minimum drain source current ($I_{d,min}$) as a function of temperature extracted from panel (a). Dashed line is a fit based on G-R limited dark current.

photoconductive gain and a strongly polarized photoresponse.[22−24]

Here, we perform a detailed characterization of gated-photoconductors based on b-P and b-PAs alloys as a function of thickness. The bandgaps of these materials were determined using absorption spectroscopy. Spectrally resolved photoresponse measurements of various compositions were performed for the first time, which are in agreement with absorption measurements. We find that while b-PAs alloys show larger bandgaps than what has been previously estimated from the extinction coefficient, this material system provides full tunability over the mid-IR band. Furthermore, we find these photoconductive detectors show a highly polarized photoresponse, with an extinction ratio >100×. Finally, we measured the responsivity and specific defectivity of these gated photoconductors using flood illumination from a blackbody source and measured a peak D^* of 6×10^{10} cm $Hz^{1/2}$ W^{-1} and 2.4×10^{10} cm $Hz^{1/2}$ W^{-1} for pure b-P and b-PAs (91% As), respectively, at room temperature.

RESULTS AND DISCUSSION

Figure 1a,b shows an optical image and cross-sectional schematic of the gated-photoconductors fabricated in this study. Multilayer b-P and b-PAs crystals with different As concentrations were exfoliated on Si/SiO_2 substrates with a 50 nm-thick oxide in a N_2 glovebox and were coated with PMMA prior to removal from the nitrogen ambient. For device fabrication, exposure to air was minimized, and critical process steps such as lift-off were performed inside a glovebox with anhydrous solvents. Measurements shown in this work were either carried out in a purged N_2 environment or under vacuum.

Material Characterization and Optical Properties. Energy dispersive electron spectroscopy (EDS) was performed to verify the compositions of the materials investigated here (EDS spectra shown in Figure S1). In addition, Raman spectroscopy was performed to verify the crystal structure and composition of the various b-PAs crystals. Raman spectra for b-P and b-PAs crystals are shown in Figure 1c. For bP-As (91% As), we observe Raman modes at 235.7, 247.1, and 267.1 cm^{-1}, corresponding to the out-of-plane A_g^1 mode, in-plane B_{2g} mode, and out-of-plane A_g^2 mode of b-As, respectively. Additionally, for b-PAs we observe additional peaks over the range of 300−400 cm^{-1}, which have been attributed to varied P-P/As-P/P-As bonding for the alloyed materials. These spectra are consistent with the findings of Liu *et al.*, who performed both Raman measurements as well as calculations on the expected vibrational modes of b-PAs.[18,20]

Transmission and reflection measurements were performed for crystals transferred onto KBr substrates to determine the bandgap of b-PAs alloys. Polarization resolved transmission and reflection spectra for a b-PAs (91% As) crystal, taken using a Fourier transform infrared spectrometer (FTIR) microscope, are shown in Figure 2a,b, respectively. The optical path was kept constant for both measurements, and reflection spectra were taken in reference to an Au mirror. From these measurements, we can obtain the absorption coefficient, calculated as 100% reflection−transmission as shown in Figure 2c. We observe strongly polarized light absorption along the perpendicular crystal direction, which is consistent with previous reports.[17] The absorption as a function of polarization angle at a wavelength of 3.5 μm is shown in the inset of Figure 2c. The bandgap as a function of composition is extracted from the absorption spectra and shown in Figure 2d (absorption measurements on various compositions are shown in Figure S2). The bandgap (E_g) of this material system can be tuned from 3.8 μm (326 meV) for pure b-P to 4.6 μm (269 meV) for b-PAs (91% As). It is worthwhile to note that previous measurements on the extinction coefficient of b-PAs alloys suggested a potentially wider range of bandgap tunability (E_g = 150 meV for b-PAs 83% As).[18] This discrepancy can be attributed to utilizing the extinction coefficient to extract E_g, which does not account for reflected light at wavelengths below the bandgap, as can be seen in Figures 2a and S3.

Dark Current Mechanism. A critical roadblock for IR detectors is the significant dark current arising from small bandgaps, which places a limit on the noise of the device.[25] Ultimately for mid- and long-wave IR detectors, the performance limit is set by random variations in the background radiation viewed by the device.[25] A key advantage of utilizing an

DOI: 10.1021/acsnano.7b07028
ACS Nano XXXX, XXX, XXX−XXX

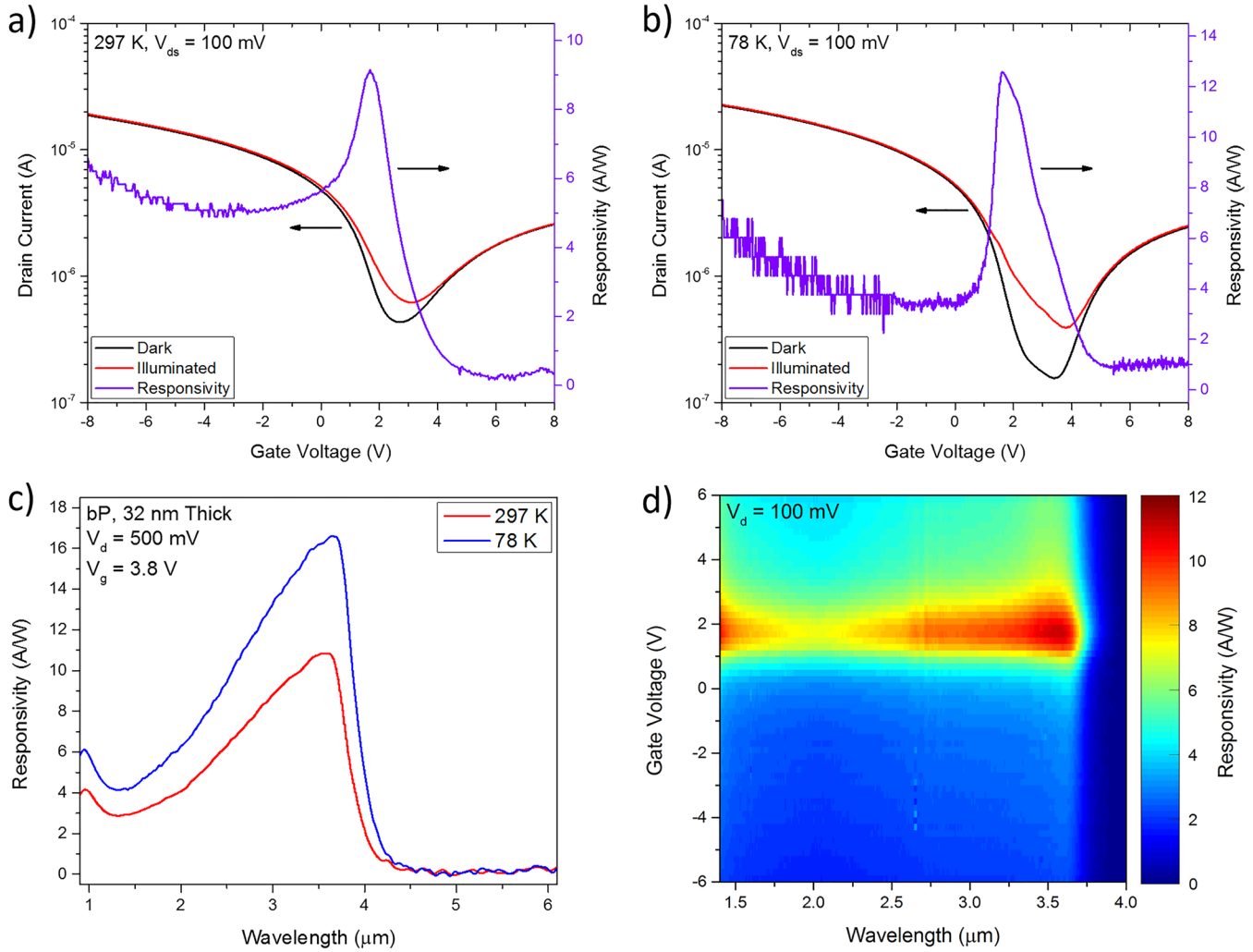

Figure 4. (a) Transfer characteristics of a 29 nm-thick b-P gated photoconductor measured under dark and illumination from a 1000 K blackbody with the device at 297 K. (b) Transfer characteristics of a 29 nm-thick b-P gated photoconductor measured under dark and illumination from a 1000 K blackbody with the device at 77 K. Note that a cold shield was not present for dark measurements. (c) Broadband spectral photoresponse of the device shown in (a) and (b), measured at 297 and 77 K. (b) Gate voltage dependence of the spectral photoresponse, measured at 297 K.

ultrathin material as the active detector is that the active volume which contributes to thermal generation is reduced per unit area of the device. In addition, for ultrathin devices, the background doping concentration in the semiconductor can be electrostatically tuned with the gate. To understand the source of the noise current as a function of gate voltage for b-P, we performed temperature-dependent measurements of the conductance. As shown in Figure 3a, we observe a minimum in the dark current at small, positive gate voltages, which indicates that the material is lightly p-doped. Additionally, we see that the Ni contact to these devices is ambipolar indicating that it can inject both electrons and holes. The minimum dark current, corresponding to the gate voltages where the background doping is compensated, is plotted in Figure 3b. The current from carrier generation-recombination (G-R), $I_{G\text{-}R}$, is proportional to

$$I_{G\text{-}R} \propto T^{3/2} \exp(-E_{g,0}/2kT) \quad (1)$$

where T is the temperature, $E_{g,0}$ is the effective bandgap, and k is the Boltzmann constant.[26] By fitting the $I_{d,min}$ to the G-R current, we extract an effective bandgap of 305 meV. This is in reasonable agreement with values extracted from absorption measurements (326 meV) and is expected to underestimate the bandgap due to contributions from trap states.

Gate Voltage Dependence of Responsivity. Figure 4a,b shows transfer characteristics of a typical 31 nm-thick b-P gated photoconductor taken in the dark and under illumination by a 1000 K blackbody with the detector held at 297 and 77 K, respectively. The corresponding responsivity, R, is also shown, calculated as $I_l - I_d/P$, where I_l current measured with the detector illuminated by a 1000 K blackbody, I_d is the current measured with the device viewing a room temperature background, and P is total incident power above the band-edge. From both the transfer characteristics and the photo-response curves it can readily be seen that the optimum photoresponse is obtained when the device is gated to compensate the background doping electrostatically. The spectral photoresponse of the b-P photoconductor was measured using the experimental setup shown in Figures S4 and S5. Here, illumination from the same 1000 K blackbody is modulated using a FTIR spectrometer, and the measured spectra at 77 and 297 K (at a gate voltage of 3.8 V) are shown

DOI: 10.1021/acsnano.7b07028
ACS Nano XXXX, XXX, XXX−XXX

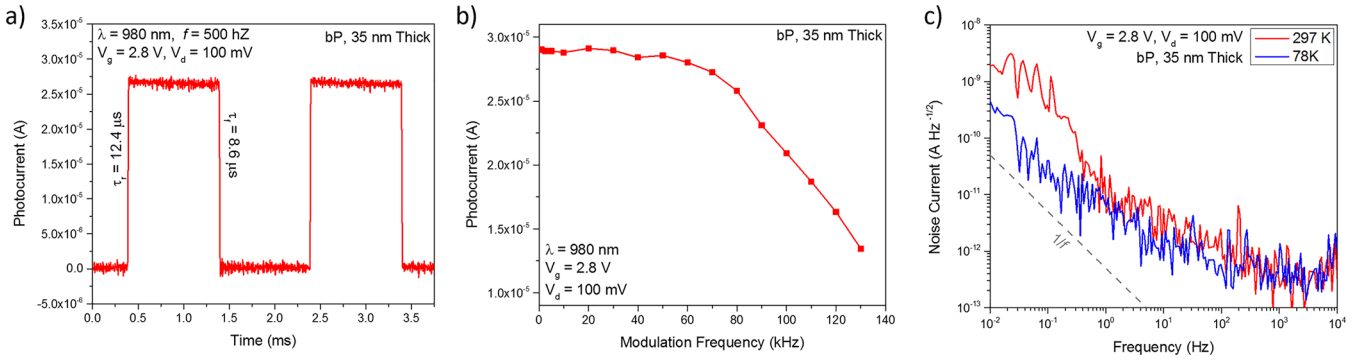

Figure 5. (a) Room-temperature temporal photoresponse of a 35 nm-thick b-P photoconductor, excited by a 980 nm laser modulated at 50 kHz. (b) Photocurrent *versus* modulation frequency measured at an incident power of 15 nW measured at room temperature, showing a 3 dB frequency of 117 kHz. (c) Noise spectrum measured for a 35 nm-thick b-P photoconductor at room temperature and 77 K; dashed line shows a reference $1/f$ curve.

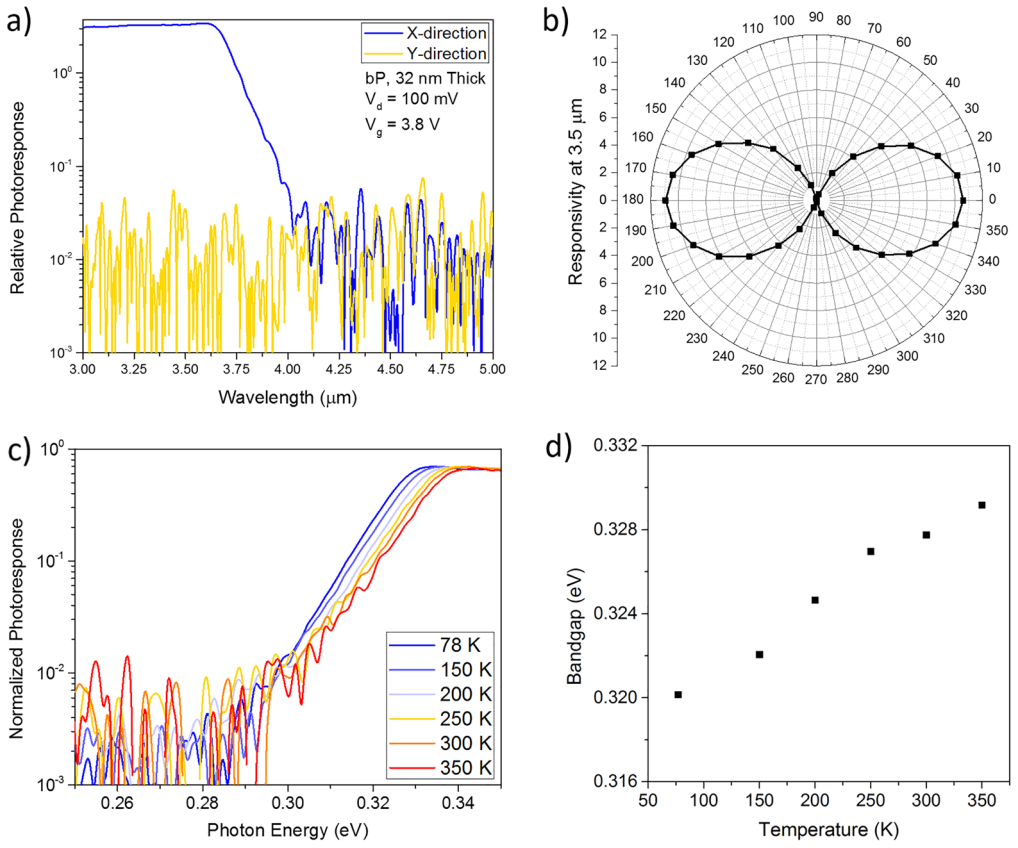

Figure 6. (a) Relative response of a b-P photoconductor measured for incident light polarized along (x-direction, arm-chair) and perpendicular to (y-direction, zigzag) the absorbing axis of the b-P crystal. (b) Responsivity of the device shown in panel (a) as a function of polarizer angle. (c) Normalized photoresponse of a b-P photodetector measured as a function of temperature. (d) Extracted bandgap from the spectral photoresponse as a function of device temperature.

in Figure 4c. The gate-dependent photoresponse extracted from spectral response measurements is shown in Figure 4d and is in good agreement with the measurements shown in Figure 4a,b. We can observe a clear absorption edge for the b-P detector, corresponding to the material's bandgap. The cutoff wavelength, λ_{co} (defined as wavelength at which responsivity drops by 50%), for this device at room temperature is 3.91 μm and is in very good agreement with the E_g value fitted from reflection/transmission measurements.

Frequency Response, Photoconductive Gain, and Noise Current. The frequency response as well as the rise and fall time were measured using a directly modulated laser diode (λ = 980 nm) and are shown in Figure 5a,b. We measure a rise and fall time of 12.4 and 8.6 μs, respectively. The 3 dB bandwidth is extracted from Figure 5b to be 117 kHz. From this analysis, we can estimate the photocarrier lifetime, τ_0, from $f_{3\ dB} = 1/2\pi\tau_0$ to be 1.4 μs. Additionally, we can calculate the carrier transit time, τ_{tr}, from the field-effect mobility (μ_{fe}) for this device (596 cm^2 V^{-1} s^{-1}) which is estimated using $\mu_{fe} = (dI_d/dV_g)(L/W)/(V_dC_{ox})$, where L, W, and C_{ox} are the length, width, and oxide capacitance of the device, respectively. Subsequently, the τ_{tr} is calculated to be 8.2 ns using $\tau_{tr} = L^2/$

DOI: 10.1021/acsnano.7b07028
ACS Nano XXXX, XXX, XXX−XXX

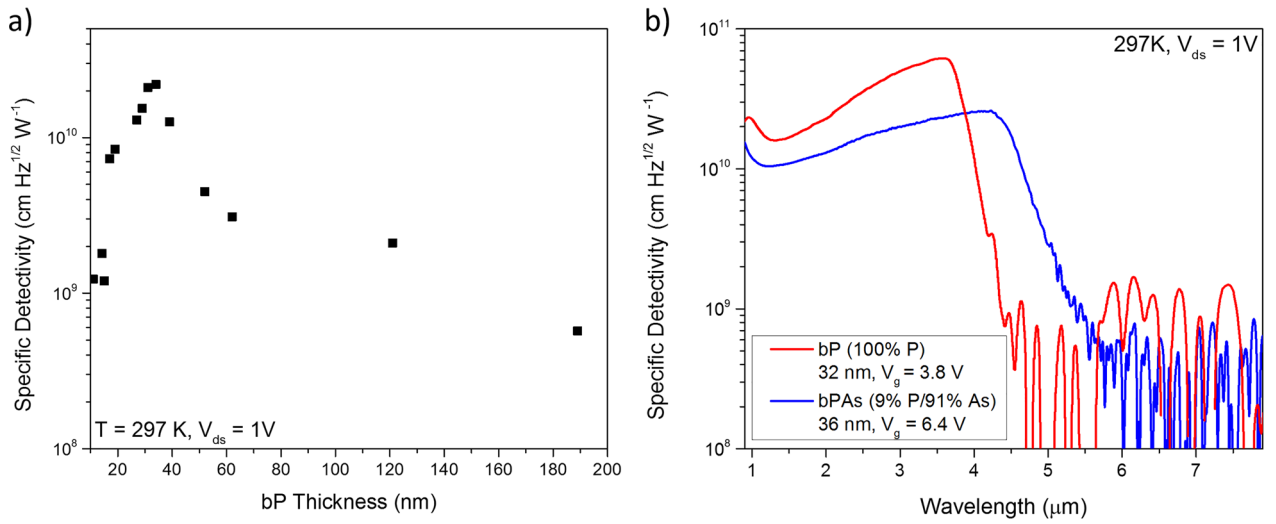

Figure 7. (a) Specific detectivity of b-P photoconductors as a function of layer thickness; measurements were performed under gating conditions which maximized the detectivity for the specific device at room temperature. (b) Specific detectivity of b-P and b-PAs photoconductors with optimized thickness; measurements were performed under gating conditions which maximized detectivity for the specific device at room temperature.

$(\mu_{fe}V_d)$. From this we can estimate the photoconductive gain (G) to be 54 at a bias voltage of V_d = 100 mV.

The quantum efficiency of the device can be calculated utilizing the measured responsivity and the gain according to

$$R(\lambda) = \frac{q\eta\lambda G}{\hbar c} \tag{2}$$

where q is the electron charge, η is the quantum efficiency, $\hbar$ is Planck's constant, and c is the speed of light.[27] We obtain a quantum efficiency of 6.4% for unpolarized incident light. This value is found to be reasonable based on reflection measurements taken on the same device, which indicates that ~8% of incident light is absorbed by the device at λ = 980 nm and is thus able to contribute to the photocurrent.

The noise current density for a typical device operated at $I_{d,min}$ as a function of frequency (f) is shown at room temperature and 77 K in Figure 5c. We can observe that the low-frequency behavior (f < 150 Hz) is dominated by $1/f$ flicker noise both at room temperature and 77 K.[27,28] This behavior is often observed in photoconductive detectors as well as in previous b-P transistors and photoconductors and is attributed to charge trapping/detrapping. At moderate frequencies, the total noise current is the sum of contributions from Shot, G-R, and Johnson noise. For this device under low intensity illumination, Shot noise is expected to dominate (as can be seen from temperature-dependent measurements in Figure 3b) and is given as $i_S^2 = 2qI_{G\text{-}R}\Delta f$, where q and $I_{G\text{-}R}$ are the electron charge and G-R current respectively.[28,29]

Polarization Resolved and Temperature-Dependent Photoresponse. As shown previously in Figure 2c, b-P shows a highly polarized absorption, and previous studies have shown that under visible illumination b-P photoconductors show a preferential response to light polarized along the x-direction (arm-chair direction).[20,22,23] We measured the polarization dependence of a b-P gated-photoconductor by placing a linear BaF_2 wire-grid polarizer in the FTIR beam path directly in front of the b-P gated-photoconductor. As expected from the highly polarized absorption spectra of b-P, there is strong anisotropicity in the photoresponse for polarization aligned to and against the crystal orientation of the b-P. We find that the polarization ratio between the two crystal orientations at mid-infrared wavelengths is over 100×. It is important to note that this value is limited by the dynamic range of the FTIR and is approaching the extinction ratio of the polarizer used in this study. The polarization resolved photoresponse measured for 3.5 μm incident light is shown in Figure 6a,b. The spectral photoresponse, measured as a function of temperature for a b-P photoconductor is shown in Figure 6c. Interestingly, we observe that the cutoff wavelength of the device extends to lower photon energies as the temperature is reduced. While this is the opposite from the behavior typically observed in most semiconductors, it is consistent with the calculated bandgap for b-P which has been predicted to show decreasing E_g with temperature due to its negative pressure coefficient and strong electron-photon coupling.[30,31] The extracted bandgap values from the spectral photoresponse are shown in Figure 6d.

Thickness Dependence and Specific Detectivity of b-PAs Photoconductors. Finally, we investigated the specific detectivity of b-P and b-PAs photoconductors. The generic expression for specific detectivity is given by

$$D^* = \frac{\sqrt{A\Delta f}}{\mathrm{NEP}} = \frac{R\sqrt{A\Delta f}}{i_n} \tag{3}$$

where A is the detector area, Δf is the integration time, NEP is noise equivalent power, and i_n is the noise current.[27,32] In the ideal case for photoconductors, the i_n is limited by shot noise and can be calculated from dark resistance of the device. However, this generally provides a strong overestimation of D^*. For the purpose of this work we utilized the experimentally measured noise current for all D^* calculations, which are taken at a modulation frequency of 150 Hz to minimize the contribution of $1/f$ noise. The specific detectivity measured for b-P as a function of thickness under illumination by a 673 K blackbody using the setup shown in Figure S5 is shown in Figure 7a. We found that the optimum thickness for maximizing D^* was 25−35 nm-thick, which balanced the increased absorption for thicker layers and the reduced dark current and thermal-generation for thinner layers. The thickness dependence of D^* can be understood from eq 4,

DOI: 10.1021/acsnano.7b07028
ACS Nano XXXX, XXX, XXX−XXX

which assumes a constant device area, that responsivity is directly proportional to absorption in the material and the photoconductive gain is thickness independent.

$$D^* \propto \frac{\text{signal}}{\text{noise}} \propto \frac{(1 - e^{-\alpha t})}{\langle i_S^2 \rangle + \langle i_J^2 \rangle + N_e} \quad (4)$$

where α is the absorption coefficient, t is the thickness, $\langle i_J^2 \rangle$ is the Johnson noise, and N_e is excess noise. In the ideal case $\langle i_S^2 \rangle$ and $\langle i_J^2 \rangle$ are proportional to the active semiconductor thickness; however, in practice the excess noise contribution dominates in the limit case when t approaches zero, leading to an optimal device thickness. Figure 7b shows the specific detectivity as a function of wavelength for b-P and b-PAs gated photoconductors, fabricated with the optimized thickness. We obtain a peak room temperature D^* of 6×10^{10} cm $Hz^{1/2}$ W^{-1} and 2.4×10^{10} cm $Hz^{1/2}$ W^{-1} for pure b-P and b-PAs (91% As), respectively, from the measured noise current.

CONCLUSION

In summary, we have investigated the spectral performance of b-P and b-PAs gated-photoconductors as a function of thickness and composition. We find that the specific detectivity of these devices can be significantly improved by tuning the thickness. For optimized devices, with a thickness of ~28 nm, we obtain peak D^* of 6×10^{10} cm $Hz^{1/2}$ W^{-1} for b-P and 2.4×10^{10} cm $Hz^{1/2}$ W^{-1} for b-PAs (91% As) at room temperature with a bandwidth of 117 kHz. This detectivity is an order of magnitude greater than commercial devices operating at room temperature.[1−3,32] In addition these devices show very strong sensitivity to the polarization of incident light, with an extinction ratio >100× which is comparable to traditional polarization optics. However, we found from both transmission/reflection and spectrally resolved photoresponse measurements that the bandgap tunability of the b-PAs material system is smaller than what was initially estimated and is limited to mid-wave-IR spectral bands.[18] As such, other techniques of reducing the bandgap in b-PAs or new 2D materials still need to be investigated to achieve longwave-IR photodetection.

METHODS

Device Fabrication. b-P and b-PAs crystals (purchased from Smart Elements and HQ Graphene, respectively) were utilized for all devices in this study. Significant effort was made during processing to minimize exposure to ambient air, due to the hydroscopic nature of b-P. Crystals were exfoliated and spin-coated with PMMA C4 in a nitrogen glovebox on p^{+2} Si/SiO_2 chips with a 50 nm-thick gate oxide. Following exfoliation and encapsulation with PMMA, suitable crystals were located by using an optical microscope, and devices were fabricated using standard e-beam lithography techniques. After development, 40 nm-thick Ni electrodes were deposited by thermal evaporation, and lift-off was performed using anhydrous solvents in a nitrogen glovebox. The sample thickness was then measured in an N_2 purged AFM (Bruker), and devices were subsequently wire bonded in a 24 pin chip carrier. Samples for absorption/reflection measurements were transferred to KBr substrates using a previously established dry transfer technique and were measured in an FTIR microscope.

Detector Characterization. Temperature-dependent electrical measurements on b-P were performed in a flow cryo probe station (Lakeshore) using a B1500A Semiconductor Parameter Analyzer (Agilent). For measurements taken in Figure 2a, a V_{ds} which was significantly lower than the bandgap of b-P (V_{ds} = 10 mV) was selected. This was done in order to ensure low-field transport, for subsequent bandgap extraction. Spectral photoresponse measurements were performed in a FTIR spectrometer (ThermoFisher), with a customized Janis cryostat using a CaF_2 window. Prior to measurement, the wire bonded devices were loaded into the spectrometer and evacuated to a base pressure of $<10^{-5}$ Torr. The cryostat was then placed at the auxiliary exit port of the FTIR, and the exciting illumination from the Glowbar (1000 K blackbody) source was focused on the sample using either a CaF_2 lens or 15× Schwarzschild objective. The photocurrent from the b-P/b-PAs devices was then sent to a current amplifier (Stanford Research Systems), which also provided the bias voltage, and the signal was subsequently returned to the external detector interface of the FTIR. All measurements taken with the FTIR were performed with the current amplifier operating with a gain setting such that the bandwidth was >100 kHz. Bias voltage and gain were selected to maximize signal-to-noise ratio for the particular device under measurement, with the aforementioned condition. During measurements, the gate bias of the device was pulsed synchronously with the FTIR, as shown in Figure S4, in order to mitigate hysteresis in the device. The relative intensity of the illumination source was measured using the internal deuterated triglycine sulfate (DTGS) detector of the FTIR with identical measurement conditions. Polarization measurements were performed by placing a BaF_2 wire grid polarizer in the beam path, and the polarization response of the system was calibrated using a commercial Ge and HgCdTe detector in place of the sample. The frequency response of the devices was measured using a directly modulated 980 nm laser. To measure the specific defectivity of the devices, we utilized optically chopped flood illumination from a 673 K blackbody source with no focusing optics. The net power incident on the device above the band-edge was calculated by the integration of the spectral radiant exitance of the blackbody and sample (M_{total}) according to Planck's Law:

$$M_{total}(\lambda, T) = \bar{\epsilon} \int_0^{\lambda_{co}} \frac{2\pi c}{\lambda^4 (e^{\hbar c/\lambda kT} - 1)} d\lambda \quad (5)$$

where, $\bar{\epsilon}$ is average the emissivity, T is temperature, λ is wavelength, λ_{co} is the cutoff wavelength of the detector under test, $\hbar$ is Planck's constant, k is Boltzmann's constant, and c is the speed of light. The projected solid angle viewed by the detector (Ω) is calculated as

$$\Omega = \pi \frac{r^2}{D^2 + r^2} \quad (6)$$

where r is the radius of the defining aperture and D is the distance between the aperture and sample surface. The total incident power on the detector can then be calculated according to

$$E = \frac{\Omega}{\pi} \times (M_{total,BB} - M_{total,Det}) \times M.F. \times A \quad (7)$$

where $M_{total,BB}$ is the integrated photon exitance of the blackbody, $M_{total,Det}$ is the integrated photon exitance of the detector, $M.F.$ is the chopper modulation factor, and A is the device area. The photocurrent and noise current in the device was then measured using a lock-in amplifier. For all measurements, an integration time of 1s was used, and the blackbody was chopped at a frequency of 150 Hz.

ASSOCIATED CONTENT

Supporting Information

The Supporting Information is available free of charge on the ACS Publications website at DOI: 10.1021/acsnano.7b07028.

Additional absorption measurements on b-P and b-PAs. Schematic of the optical setups used for characterization of photodetectors and gating scheme used to minimize hysteresis (PDF)

AUTHOR INFORMATION

Corresponding Author

*E-mail: ajavey@berkeley.edu.

DOI: 10.1021/acsnano.7b07028
ACS Nano XXXX, XXX, XXX−XXX

ORCID

Matin Amani: 0000-0002-7912-6559

Ali Javey: 0000-0001-7214-7931

Notes

The authors declare no competing financial interest.

ACKNOWLEDGMENTS

The authors would like to acknowledge P. Wijewarnasuriya and E. DeCuir from the U.S. Army Research Laboratory for their discussions. This work was supported by the Defense Advanced Research Projects Agency under contract no. HR0011-16-1-0004. Raman spectroscopy was supported by the U.S. Department of Energy, Office of Science, Office of Basic Energy Sciences, Materials Sciences and Engineering Division under contract no. DE-AC02-05CH11231 within the Electronic Materials Program (KC1201).

REFERENCES

(1) Razeghi, M.; Nguyen, B.-H. Advances in Mid-Infared Detection and Imaging: A Key Issues Review. *Rep. Prog. Phys.* **2014**, *77*, 77−082401.

(2) Barve, A. V.; Lee, S. J.; Noh, S. K.; Krishna, S. Review of Current Progress in Quantum Dot Infrared Photodetectors. *Laser Photon. Rev.* **2010**, *4*, 738−750.

(3) Piotrowski, J.; Rogalski, A. Uncooled Long Wavelength Infrared Photon Detectors. *Infrared Phys. Technol.* **2004**, *46*, 115−131.

(4) Kimukin, I.; Biyikli, N.; Ozbay, E. InSb High-Speed Photodetectors Grown on GaAs Substrates. *J. Appl. Phys.* **2003**, *94*, 5414−5416.

(5) Norton, P. HgCdTe Infrared Detectors. *Opto-Electron. Rev.* **2002**, *10*, 159−174.

(6) Hoang, A. M.; Dehzangi, A.; Adhikary, S.; Razeghi, M. High Performance Bias-Selectable Three-Color Short-Wave/Mid-Wave/Long-Wave in Infrared Photodetectors Based on Type-II InAs/GaSb/AlSb Superlattices. *Sci. Rep.* **2016**, *6*, 24144.

(7) Niklaus, F.; Vieider, C.; Jakobsen, H. *Proc. SPIE* **2007**, *6836*, 68360D−1.

(8) Rogalski, A. HgCdTe Infrared Detector Material: History, Status and Outlook. *Rep. Prog. Phys.* **2005**, *68*, 2267−2336.

(9) Xia, F.; Wang, H.; Xiao, D.; Dubey, M.; Ramasubramaniam, A. *Nat. Photonics* **2014**, *8*, 899−907.

(10) Lin, Z.; McCreary, A.; Briggs, N.; Subramanian, S.; Zhang, K.; Sun, Y.; Li, X.; Borys, N. J.; Yuan, H.; Fullerton-Shirey, S. K.; Chernikov, A.; Zhao, H.; McDonnell, S.; Lindenberg, A. M.; Xiao, K.; LeRoy, B. J.; Drndic, M.; Hwang, J. C. M.; Park, J.; Chhowalla, M.; et al. 2D Materials Advances: From Large Scale Synthesis and Controlled Heterostructures to Improved Characterization Techniques, Defects and Applications. *2D Mater.* **2016**, *3*, 3−042001.

(11) Amani, M.; Lien, D.-H.; Kiriya, D.; Xiao, J.; Azcatl, A.; Noh, J.; Madhvapathy, S. R.; Addou, R.; Kc, S.; Dubey, M.; Cho, K.; Wallace, R. M.; Lee, S.-C.; He, J.-H.; Ager, J. W.; Zhang, X.; Yablonovitch, E.; Javey, A. Near-Unity Photoluminescence Quantum Yield in MoS_2. *Science* **2015**, *350*, 1065−1068.

(12) Amani, M.; Taheri, P.; Addou, R.; Ahn, G. H.; Kiriya, D.; Lien, D.-H.; Ager, J. W.; Wallace, R. M.; Javey, A. Recombination Kinetics and Effects of Superacid Treatment in Sulfur- and Selenium Based Transition Metal Dichalcogenides. *Nano Lett.* **2016**, *16*, 2786−2791.

(13) Koppens, F. H. L.; Mueller, T.; Avouris, P. H.; Ferrari, C.; Vitiello, M. S.; Polini, M. Photodetectors Based on Graphene, Other Two-Dimensional Materials, and Hybrid Systems. *Nat. Nanotechnol.* **2014**, *9*, 780−793.

(14) Zhang, Y.; Liu, T.; Meng, B.; Li, X.; Liang, G.; Hu, X.; Wang, Q. J. Broadband High Photoresponse from Pure Monolayer Graphene Photodetector. *Nat. Commun.* **2013**, *4*, 1811.

(15) Liu, C.-H.; Chang, Y.-C.; Norris, T. B.; Zhong, Z. Graphene Photodetectors with Ultra-Broadband and High Responsivity at Room Temperature. *Nat. Nanotechnol.* **2014**, *9*, 273−278.

(16) Yan, J.; Kim, M.-H.; Elle, J. A.; Sushkov, A. B.; Jenkins, G. S.; Milchberg, H. M.; Fuhrer, M. S.; Drew, H. D. Dual-Gated Bilayer Graphene Hot-Electron Bolometer. *Nat. Nanotechnol.* **2012**, *7*, 472−478.

(17) Ling, X.; Wang, H.; Huang, S.; Xia, F.; Dresselhaus, M. S. The Renaissance of Black Phosphorus. *Proc. Natl. Acad. Sci. U. S. A.* **2015**, *112*, 4523−4530.

(18) Liu, B.; Kopf, M.; Abbas, A. N.; Wang, X.; Guo, Q.; Jia, Y.; Xia, F.; Weihrich, R.; Bachhuber, F.; Pielnhofer, F.; Wang, H.; Dhal, R.; Cronin, S. B.; Ge, M.; Fang, X.; Nilges, T.; Zhou, C. Black Arsenic-Phosphorus: Layered Anisotropic Infrared Semiconductors with Highly Tunable Compositions and Properties. *Adv. Mater.* **2015**, *27*, 4423−4429.

(19) Qiao, J.; Kong, X.; Hu, Z.-X.; Yang, F.; Ji, W. High-Mobility Transport Anisotropy and Linear Dichroism in Few-Layer Black Phosphorous. *Nat. Commun.* **2014**, *5*, 4475.

(20) Wang, X.; Jones, A. M.; Seyler, K. L.; Tran, V.; Jia, Y.; Zhao, H.; Wang, H.; Yang, L.; Xu, X.; Xia, F. Highly Anisotropic and Robust Excitons in Monolayer Black Phosphorus. *Nat. Nanotechnol.* **2015**, *10*, 517−521.

(21) Tran, V.; Soklaski, R.; Liang, Y.; Yang, L. Layer-Controlled Band Gap and Anisotropic Few-Layer Black Phosphorous. *Phys. Rev. B: Condens. Matter Mater. Phys.* **2014**, *89*, 235319.

(22) Guo, Q.; Pospischil, A.; Bhuiyan, M.; Jiang, H.; Tian, H.; Farmer, D.; Deng, B.; Li, C.; Han, S.-J.; Wang, H.; Xia, Q.; Ma, T.-P.; Mueller, T.; Xia, F. Black Phosphorus Mid-Infrared Photodetectors with High Gain. *Nano Lett.* **2016**, *16*, 4648−4655.

(23) Yuan, H.; Liu, X.; Afshinmanesh, A.; Li, W.; Xu, G.; Sun, J.; Lian, B.; Curto, A. G.; Ye, G.; Hikita, Y.; Shen, Z.; Zhang, S.-C.; Chen, X.; Brongersma, M.; Hwang, H. Y.; Cui, Y. Polarization-Sensitive Broadband Photodetector using a Black Phosphorus Vertical p-n Junction. *Nat. Nanotechnol.* **2015**, *10*, 707−713.

(24) Miao, J.; Zhang, S.; Cai, L.; Wang, C. Black Phosphorus Schottky Diodes: Channel Length Scaling and Application as Photodetectors. *Adv. Electron. Mater.* **2016**, *2*, 1500346.

(25) Piotrowski, J.; Gawron, W. Ultimate Performance of Infrared Photodetectors and Figure of Merit of Detector Material. *Infrared Phys. Technol.* **1997**, *38*, 63−68.

(26) Martyniuk, P.; Antoszewski, J.; Martyniuk, M.; Faraone, L.; Rogalski, A. New Concepts in Infrared Photodetector Designs. *Appl. Phys. Rev.* **2014**, *1*, 1−041102.

(27) Petritz, R. L. Theory of Photoconductivity in Semiconductor Film. *Phys. Rev.* **1956**, *104*, 1508−1516.

(28) Beck, W. A. Photoconductive Gain and Generation-Recombination Noise in Multiple-Quantum-Well Infrared Detectors. *Appl. Phys. Lett.* **1993**, *63*, 3589−3591.

(29) Ye, Z.; Campbell, J. C.; Chen, Z.; Kim, E.-T.; Madhukar, A. Noise and Photoconductive Gain in InAs Quantum-Dot Infrared Photodetectors. *Appl. Phys. Lett.* **2003**, *83* (6), 1234−1236.

(30) Villegas, C. E. P.; Rocha, A. R.; Marini, A. Anomalous Temperature Dependence of the Band Gap in Black Phosphorus. *Nano Lett.* **2016**, *16*, 5095−5101.

(31) Villegas, C. E. P.; Rodin, A. S.; Carvalho, A.; Rocha, A. R. Two-Dimensional Exciton Properties in Monolayer Semiconducting Phosphorus Allotropes. *Phys. Chem. Chem. Phys.* **2016**, *18*, 27829.

(32) Vincent, J. D. *Fundamentals of Infrared Detector Operation and Testing*; Wiley: New York, 1990.

DOI: 10.1021/acsnano.7b07028
ACS Nano XXXX, XXX, XXX−XXX

Supporting Information For

Mid-Wave Infrared Photoconductors Based on Black Phosphorous-Arsenic Alloys

Matin Amani[1,2], *Emma Regan*[1,2], *James Bullock*[1,2], *Geun Ho Ahn*[1,2], *and Ali Javey*[1,2,*]

[1]Electrical Engineering and Computer Sciences, University of California at Berkeley, Berkeley, CA 94720, United States
[2]Materials Sciences Division, Lawrence Berkeley National Laboratory, Berkeley, CA 94720, United States

*Address correspondence to ajavey@eecs.berkeley.edu

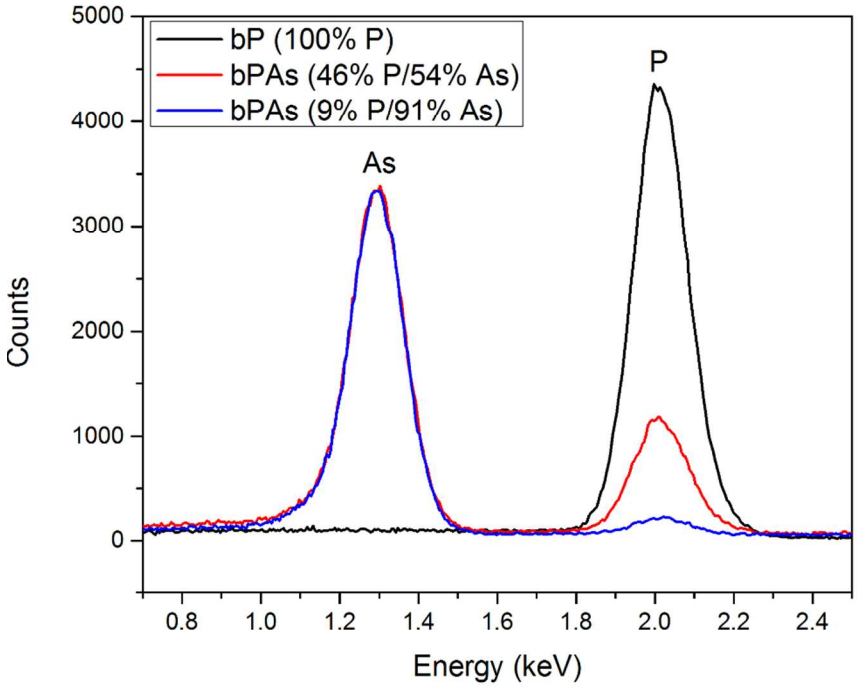

Figure S1. EDX Spectra, showing As Lα (1.282 keV) and P Kα (2.013 keV) peaks, measured for the various compositions of b-P and b-PAs studied here.

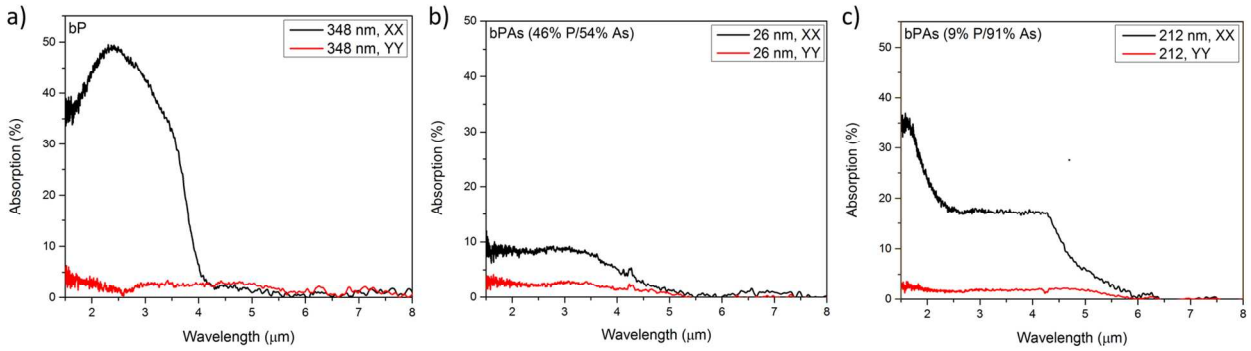

Figure S2. (a) Absorption spectra, calculated from 100-T-R in the X and Y directions measured on 348 nm thick b-P. (b) Absorption spectra, calculated from 100-T-R in the X and Y directions measured on 26 nm thick b-PAs (83% As). (c) Absorption spectra, calculated from 100-T-R in the X and Y directions measured on 212 nm thick b-PAs (91% As). Note that the total absorption is a strong function b-P/b-PAs thickness and refractive index.

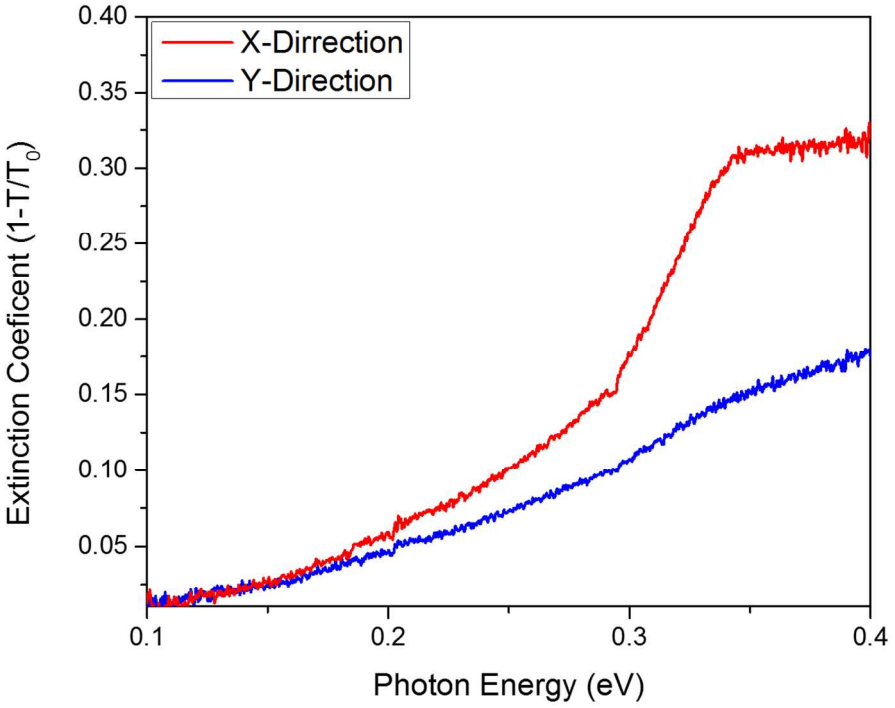

Figure S3. Extinction coefficient measured for a b-P crystal on a KBr substrate from transmission.

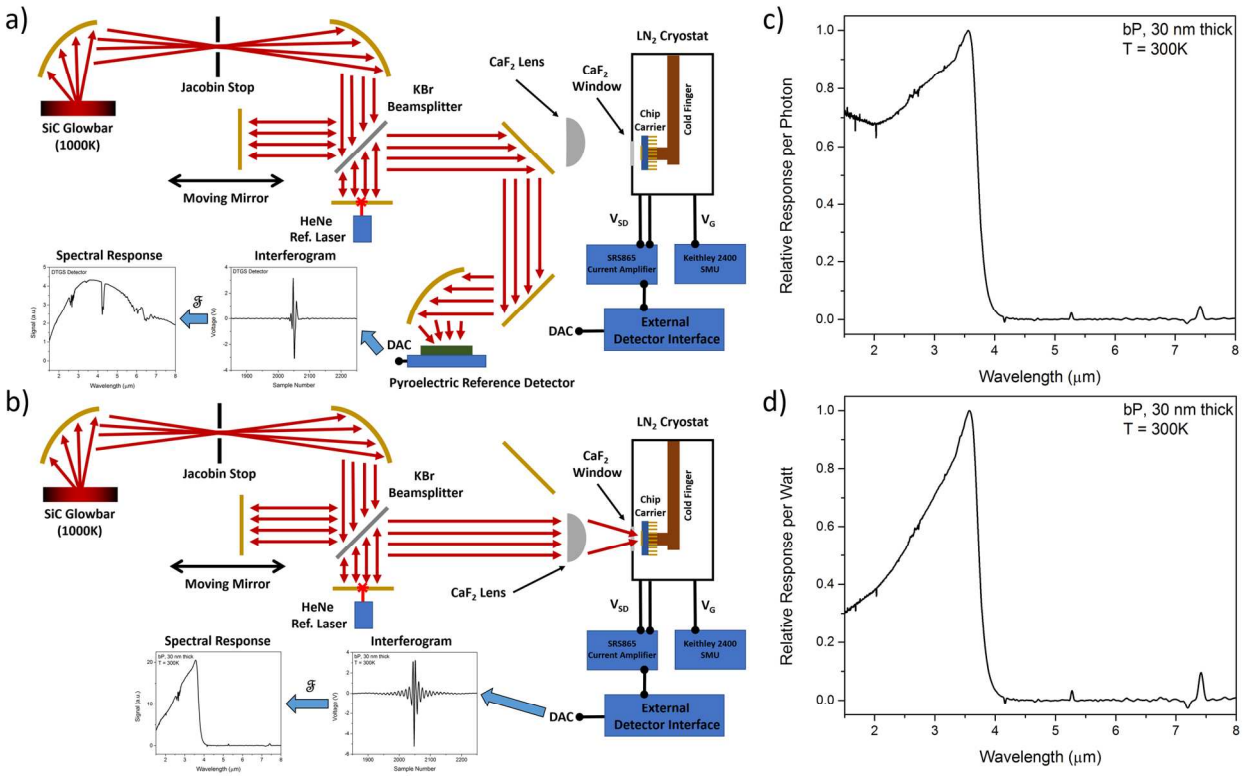

Figure S4. (a) Schematic of measurement setup used to measure the spectral content of the incident light on the b-P detector, measurements taken using the internal pyroelectric detector of the FTIR were performed at an optical velocity of 0.15 cm/s. (b) Schematic of measurement setup used to measure the spectral response of the b-P and b-PAs gated photoconductors. Light from the FTIR Glowbar was focused on the device using either a CaF2 lens or a Schwarzschild objective. During measurements, the gate voltage was modulated from V_g during the interferometer scan to -V_g during the wait period, in order to minimize hysterics effects (timing shown in Fig. S3). (c) Relative response per photon of a b-P gated photoconductor, calculated using the ratio of response from the b-P detector to the pyroelectric reference detector. (d) Relative response per photon of a b-P gated photoconductor, calculated using the ratio of response from the b-P detector to the pyroelectric reference detector and photon energy.

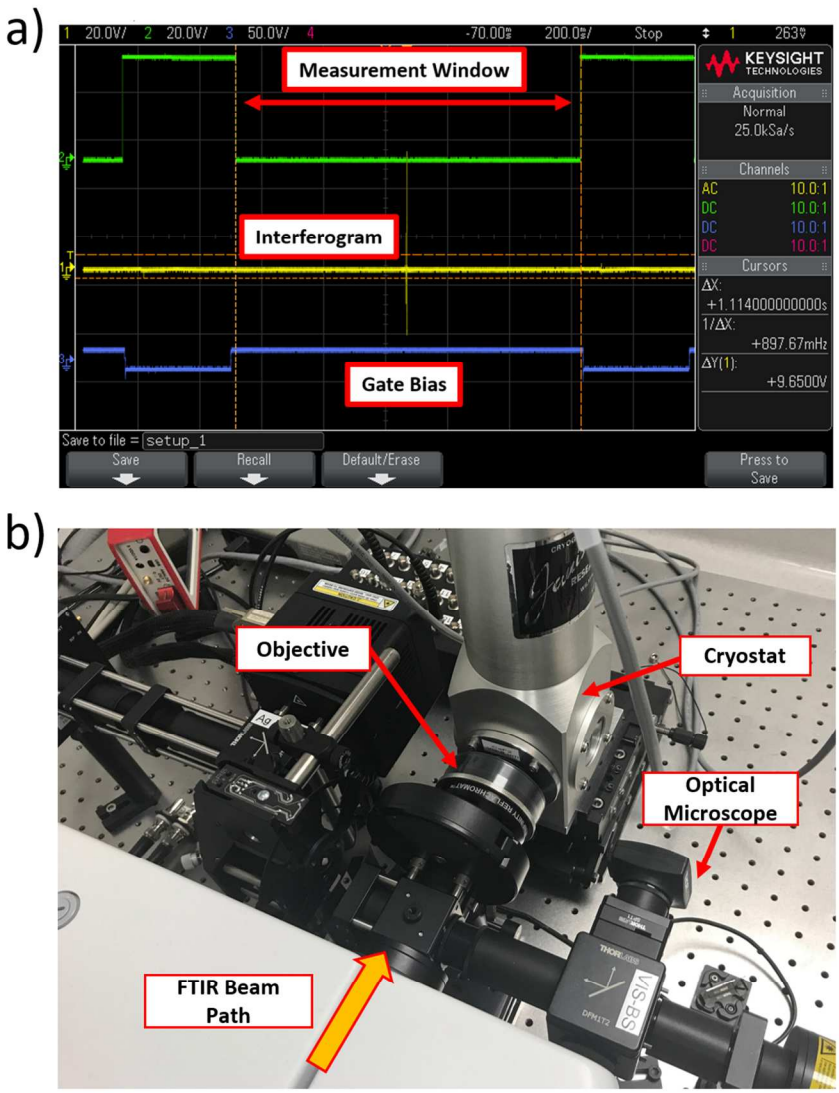

Figure S5. (a) Timing of gate biasing during FTIR measurements. During the measurement window, which is identified by an external trigger from the FTIR, the gate is held at the desired bias potential, V_g. During the rest period, the gate bias is held at -V_g, in order to minimize hysteresis effects. (b) Photograph of the optical setup used to measure the spectral and frequency response of the b-P and b-PAs gated photoconductors. Sample is placed in a 24-pin chip carrier in the cryostat. An external microscope is setup to locate and focus light on the sample with a reflective objective or CaF_2 lens.

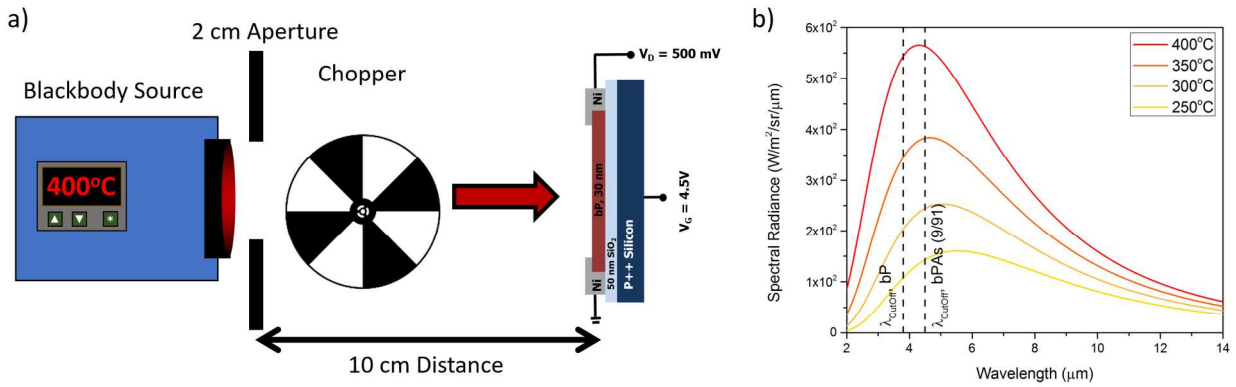

Figure S6. (a) Schematic of the setup used to measure the absolute responsivity and detectivity of the b-P detector. The sample was illuminated by a blackbody source held at 400°C-250°C (673 K-523 K). The beam was modulated using a chopper and the response of the gated photoconductor was measured using a lock-in amplifier. (b) Spectrum of the illumination on the sample at various blackbody temperatures calculated using Plank's law. The cut-off wavelengths for b-P and b-PAs (91% As) are indicated by dashed lines.